

Deriving column-integrated thermospheric temperature with the N₂ Lyman–Birge–Hopfield (2,0) band

Clayton Cantrall¹, Tomoko Matsuo¹

¹Ann and H.J. Smead Department of Aerospace Engineering Sciences, University of Colorado Boulder, Boulder, CO, USA

Correspondence to: Clayton Cantrall (clayton.cantrall@colorado.edu)

Abstract. This paper presents a new technique to derive thermospheric temperature from space-based disk observations of far ultraviolet airglow. The technique, guided by findings from principal component analysis of synthetic daytime Lyman–Birge–Hopfield (LBH) disk emissions, uses a ratio of the emissions in two spectral channels that together span the LBH (2,0) band to determine the change in band shape with respect to a change in the rotational temperature of N₂. The two-channel ratio approach limits representativeness and measurement error by only requiring measurement of the relative magnitudes between two spectral channels and not radiometrically calibrated intensities, simplifying the forward model from a full radiative transfer model to only a vibrational-rotational band model. It is shown that the derived temperature should, in general, be interpreted as a column-integrated property as opposed to a temperature at a specified altitude without utilization of a priori information of the thermospheric temperature profile. The two-channel ratio approach is demonstrated using NASA GOLD Level 1C disk emission data for the period of 2–8 November 2018 during which a small geomagnetic storm has occurred. Due to the lack of independent thermospheric temperature observations, the efficacy of the approach is validated through comparisons of the column-integrated temperature derived from GOLD Level 1C data with version 2 of the GOLD Level 2 temperature product as well as temperatures from first principle and empirical models. The storm-time thermospheric response manifested in the column-integrated temperature is also shown to corroborate well with hemispherically integrated Joule heating rates, ESA SWARM mass density at 460 km, and GOLD Level 2 column O/N₂ ratio.

1 Introduction

Remote sensing of Earth’s far ultraviolet (FUV) airglow from space provides important insights into the energetics, dynamics, and composition of the upper atmosphere (Meier et al., 1991; Paxton et al., 2017). The N₂ Lyman-Birge-Hopfield (LBH) bands (~127-280 nm) are prominent daytime FUV airglow features that emanate from the lower to middle thermosphere (~120-200 km). Currently operating instruments measuring the LBH bands include the Thermosphere-Ionosphere-Mesosphere Energetics and Dynamics (TIMED) satellite’s Global Ultraviolet Imager (GUVI) launched in 2001 (Christensen et al., 2003), the Defense Meteorological Satellite Program (DMSP) Special Sensor Ultraviolet Spectrographic Imager (SSUSI) launched in 2003 (Paxton et al., 2002), the Global-scale Observations of the Limb and Disk (GOLD) launched in 2018 (McClintock et al., 2020a), and the Ionospheric Connection Explorer’s Far UltraViolet imaging spectrograph (FUV) launched in 2019 (Mende et al., 2017).

The utility of the LBH bands for probing thermospheric temperature was demonstrated by Aksnes et al. (2006) with limb observations by the Advanced Research and Global Observation Satellite’s (ARGOS) High Resolution Ionospheric and Thermospheric Spectrograph (HITS) instrument. Eastes et al. (2008) subsequently

Deleted: LBH

Deleted: Lyman–Birge–Hopfield (

Deleted: The benefits of the two-channel ratio approach include an elimination of representativeness error as absolute LBH intensities are not required in the derivation procedure and a reduced impact of systematic measurement error caused by variations in the instrumental performance across the LBH band system as a fully resolved system is also not required.

Deleted: upon the deposition of solar extreme ultraviolet radiation...

50 showed that disk observations of LBH bands could be used for global monitoring of thermospheric temperature. These authors fit LBH laboratory spectra to observed emissions using an optimal estimation routine with varying parameters such as the N₂ rotational temperature, population rates of each vibrational band, N 149.3 nm emission intensity, O₂ photoabsorption, and background emission rates. GOLD became the first mission to provide a Level 2 data product of thermospheric temperature (T_{DISK}) using LBH disk emissions between ~132-162 nm with a similar retrieval implementation (Eastes et al., 2017). Thermospheric temperatures have also been derived from TIMED GUVI observations (Zhang et al., 2019) using an intensity ratio between the (0,0) band and (1,0) band that the authors found to be quasi-linearly dependent on the N₂ rotational temperature. The authors attributed the temperatures to the altitude at the peak of the LBH contribution function (~155 km) based on radiative transfer calculations.

Deleted: attributed to around 160 km

55

Deleted: attributed to around 155 km

60 This paper presents a new technique to derive thermospheric temperature from spectrographic measurements of FUV airglow. The technique, unlike in past work, uses the ratio of two spectral channels that span a single LBH band to determine the change in band shape with respect to a change in the rotational temperature of N₂. Section 2 provides background and exploration of the LBH temperature signal with principal component analysis (PCA) to motivate the new technique. Section 3 details the techniques implementation and provides a discussion on the error sources and a rationale behind our interpretation of the derived temperature as a column-integrated property that we refer to as column-integrated thermospheric temperature, T_{ci} . Section 4 presents the demonstrative results of applying the technique to GOLD Level 1C radiance data for the period of 2–8 November 2018; during which a small geomagnetic storm event has occurred. The derived thermospheric temperatures are compared to GOLD Level 2 T_{DISK} data product over the same period. Due to the lack of independent remotely

Deleted: FUV

Deleted: image

Moved (insertion) [1]

65 sensed or in situ temperature measurements in the lower to middle thermosphere, the derived column-integrated temperatures are also compared to (1) synthetically generated column-integrated temperatures from model simulations by NOAA's Whole Atmosphere Model (WAM) (Akmaev et al., 2011), (2) Naval Research Lab Mass Spectrometer and Incoherent Scatter Radar Extended (NRLMSISE-00) empirical model temperatures (Picone et al., 2002), and (3) observations of other thermospheric states, including GOLD Level 2 $\Sigma O/N_2$ data product (Correia et al., 2018) and mass density by ESA's SWARM constellation (Astafyeva et al., 2017) as well as hemispherically integrated Joule heating rates estimated from SuperDARN and ground-based magnetometer data by using the Assimilative Mapping of Geospace Observations (AMGeO) (AMGeO Collaboration, 2019; Matsuo, 2020).

Moved up [1]: The technique, unlike in past work, uses the ratio of two spectral channels that span a single LBH band to determine the change in band shape with respect to a change in the rotational temperature of N₂.

Deleted: ¶

The technique has a straightforward implementation that is relatively unaffected by changes in instrument performance across the LBH band system and that does not require a forward model to reproduce the absolute intensity of emissions as part of the temperature derivation procedure. These points are further elaborated in Section 3 along with a description of the technique. Section 3 also provides a discussion on potential error sources in the temperature derivation, and a rationale behind our interpretation of the derived temperature as a column-integrated property that we refer to as column-integrated thermospheric temperature, T_{ci} .

2 Temperature Signal in LBH Emissions

80 The thermospheric temperature signal is present in the rotational structure of the LBH bands. In the case of N₂, the rotational temperature is equivalent to the ambient neutral temperature (Aksnes et al., 2006). In order to motivate the new technique to extract this signal from the N₂ LBH (2,0) band, this section presents results from PCA performed on simulated LBH emissions. Synthetic LBH emission data are generated by forward modeling WAM simulation results for the period of 2–8 November 2018. WAM simulation experiments are executed with solar and geomagnetic forcing conditions specified according to the actual values of the F10.7, Kp, and hemispheric power

Deleted: principal component analysis (PCA)

Deleted: It is shown that PCA analysis helps quantify the amplitude and signal-to-noise ratio (SNR) of this temperature signal in disk LBH emission data.

Deleted: applying

Deleted: explained in Section 2.1 to

indices, solar wind velocities and densities, and interplanetary magnetic fields. Section 2.1 discusses forward modeling of LBH emissions and Section 2.2 presents the PCA results.

115 2.1 Forward Modeling of LBH Emissions

The forward model used to produce synthetic LBH emissions is built with the Global Airglow Model (GLOW) and a radiative transfer model (Solomon, 2017). GLOW computes LBH volume emission rates as a function of altitude that are input into the radiative transfer model to produce line-of-sight emissions of the LBH band system. The most important component of the forward model for the purposes of deriving thermospheric temperatures is the LBH vibrational-rotational band model (Budzien et al., 2001). The band model is a look-up table of laboratory spectra that specifies, for a given temperature, a unique spectrum for the upper vibrational states $v'=0-9$ of N_2 . In the current implementation of the forward model, the $v'=0-9$ vibrational population rates are those provided in Ajello et al. (2020) that are based on GOLD observations and are held constant. The population rate distribution can vary with the energy distribution of the electron flux in addition to variation in excitation sources other than direct excitation such as radiative cascade and collision-induced electronic transition (Ajello et al., 2020; Eastes et al., 2000a,b; Ajello et al., 1985). Ajello et al. (1985) states that excitation thresholding should be included in airglow models to accurately reproduce LBH band intensity. However, as discussed in the following section, absolute band intensity is not needed to extract the N_2 rotational temperature.

Deleted: The two primary mechanisms generating LBH emissions are direct excitation from the N_2 ground state by photoelectron impact and radiative and collisional cascading between the singlet states (Eastes et al., 2000a). GLOW currently does not consider cascading effects for the LBH vibrational states (Solomon, 2017). Eastes et al. (2000b) showed that cascading increases the total LBH emission by a factor of ~ 1.6 . The primary extinction source of LBH emissions is O_2 photoabsorption, computed line-by-line in the radiative transfer model. Figure 1 displays typical LBH contribution functions with solar zenith angle (SZA) generated by the forward model. ¶

Deleted: LBH

Deleted: In the current implementation of the forward model, the $v'=0-9$ vibrational population rates are defined by a Franck-Condon based theoretical model and are held constant (Ajello et al., 1985; Ajello et al., 2020). Ajello et al. (1985) states that significant deviations from a Franck-Condon factor distribution can occur in planetary dayglow or aurora due to the energy distribution of the electron flux, and that excitation thresholding should be included in airglow models to accurately reproduce LBH band intensity. However, as discussed in the following section, band intensity is not needed to extract the N_2 rotational temperature. ¶

130 2.2 PCA of Simulated LBH Emissions

PCA is a data reduction technique that is useful for identifying the dominant orthogonal modes of variability from data. PCA is applied here using eigenvalue decomposition of a sample covariance matrix, $S_{\lambda\lambda}$, of simulated LBH emissions, $I_{LBH_i}^s$, at wavelengths, λ , computed from aggregated data sets of simulated emissions of the LBH band system during 2–8 November 2018 for a total of $N = 8.1 \times 10^4$ samples.

$$135 \quad S_{\lambda\lambda} = \frac{1}{N-1} \sum_{i=1}^N I_{LBH_i}^{s'} T I_{LBH_i}^{s'}$$

$$I_{LBH_i}^{s'} = I_{LBH_i}^s - \overline{I_{LBH}^s}$$

$\overline{I_{LBH}^s}$ is the mean LBH spectrum of the N samples. The useful results of PCA for this investigation are a set of eigenvectors (principal components), \mathbf{v} , that describe the mode of variability in the LBH band system, with associated eigenvalues, σ . Suppose that \mathbf{v} is an orthonormal set of spatiotemporally invariant basis and spatiotemporal dependent coefficients, \mathbf{c} , represent the amplitude of the mode for each disk emission sample at a given time, t_i , and location, r_i , then $I_{LBH_i}^{s'}$ can be expressed:

$$140 \quad I_{LBH_i}^{s'}(\lambda, r_i, t_i) = c_1(r_i, t_i) \mathbf{v}_1(\lambda) + c_2(r_i, t_i) \mathbf{v}_2(\lambda) + \dots + c_n(r_i, t_i) \mathbf{v}_n(\lambda) + \mathbf{d}'(\lambda, r_i, t_i)$$

where $\mathbf{d}'(\lambda, \mathbf{r}, t)$ is the residual after subtracting the mean and the sum of n weighted modes from \mathbf{I}_{LBH}^s . The total variance of \mathbf{c} matches σ^2 for that mode.

Figure 1 shows the mean of simulated LBH radiance, $\overline{I_{LBH}^s}$, between 138–162 nm with a spectral sampling of 0.04 nm along with the first two leading modes of variability in the spectrum, ν_B and ν_T , scaled by their eigenvalues or total standard deviations, σ_B and σ_T . The leading mode ν_B is identified as the overall scaling of the LBH intensity. The value of σ_B^2 suggests that this mode accounts for 98.3% of the total variability in the simulated LBH spectra. The second leading mode ν_T is identified as the temperature signal. According to the value of σ_T^2 this secondary mode accounts for 1.6% of the total variability in the simulated LBH spectra. The correlation coefficient, R , between time-dependent coefficients for this temperature mode c_T and the simulated WAM temperatures at 155 km altitude over the course of 2–8 November 2018 is 0.71. Together these two principal components account for 99.9% of the variability in the simulated LBH spectra suggesting the LBH system is highly compressible.

Figure 2 focuses on the LBH (2,0) band identified in Fig. 1. Compared to the other LBH bands the (2,0) band is relatively bright and is isolated from the even brighter O emissions at 130.4 nm and 135.6 nm and the N emission at 149.3 nm (not shown in Fig. 1). The temperature signal in LBH emissions is apparent in the morphological shape of ν_T displayed in Fig. 2. As the rotational temperature, $T_{r,2}$, of N_2 increases there is an effective skewing of the LBH (2,0) band to longer wavelengths. The close inspection of ν_T indicates that LBH (2,0) band emissions at wavelengths above 138.58 nm are positively correlated with temperature while those below are negatively correlated. Emissions at 138.58 nm are not affected by temperature variability so have zero amplitude in ν_T . This observation substantiates an approach of binning the LBH (2,0) band into two channels using 138.58 nm as a boundary to preserve how the temperature signal manifests in the LBH emission's morphological shape. Channel A is defined as the sum of all wavelengths negatively correlated with temperature ($\sum_{\lambda=138.0}^{138.56} I_{\lambda}$), and channel B contains all wavelengths positively correlated with temperature ($\sum_{\lambda=139.2}^{138.56} I_{\lambda}$). The two channel ratio B/A is a linear function of temperature. A similar two-channel ratio approach was adopted in Cantrall et al. (2019) for testing the feasibility of assimilating GOLD Level 1C data into the WAM but a justification of such an approach was not provided.

3 Determination of Column-integrated Temperature from LBH (2,0) Band

This section details the derivation of column-integrated thermospheric temperature, T_{ci} , from the N_2 rotational structure observed in top-of-atmosphere LBH emissions using the ratio of two channels that together span the LBH (2,0) band as motivated in Section 2. Section 3.1 explains the step-by-step procedure, followed by a discussion on potential error sources of T_{ci} in Section 3.2 and analysis in Section 3.3 that supports the interpretation of T_{ci} as a column-integrated temperature rather than a temperature attributed to a specific altitude.

3.1 Procedure

The procedure consists of four steps as follows:

1. Generate synthetic data of spectrally resolved LBH (2,0) band emissions for a range of temperature using the vibrational-rotational band model.

Deleted: PCA is a data reduction technique that is useful for identifying the dominant orthogonal modes of variability from data. PCA is applied here using eigenvalue decomposition on aggregated data sets of simulated emissions of the LBH band system, I_{LBH}^s , during 2–8 November 2018 for a total of 8.1×10^4 samples. The useful results of PCA for this investigation are a set of eigenvectors (principal components), ν , that describe the mode of variability with associated eigenvalues, σ . Suppose that ν is time-invariant and time-dependent coefficients, c , represent the amplitude of the mode for each disk emission sample at a given time, where the total variance of c matches σ^2 for that mode.

Deleted: due to changes in solar and geomagnetic conditions, solar zenith angle (SZA), and emission angle

Deleted: (as explained later).

Deleted: and is just 3% of the intensity of an LBH band.

Deleted: 60

Deleted: 68

Deleted: Together these two principal components account for 99.9% of the variability in the simulated LBH spectra. Figure 1 highlights that variability of the simulated LBH disk emission spectra can be represented in a small number of degrees of freedom (i.e., there is a significant amount of redundant information) and that the temperature signal is considerably weaker than the overall LBH intensity.

Deleted: from the LBH band system shown

Deleted: Figure 2 shows ν_T scaled by σ_T along with the amplitude of shot noise, $\sqrt{I_{LBH(2,0)}^s}$. The magnitude of temperature mode ν_T is less than the level of shot noise ($SNR \approx 0.35$), underscoring the need for denoising approaches to detect the temperature signal with sufficient SNR. A simple way to improve SNR, at the cost of spectral or spatial resolution, is with binning.

Deleted: manifests as the second leading mode of emission variability as

Deleted: The

Deleted: In this study, the LBH (2,0) band is sampled at 0.04 nm resulting in 30 bins over 138.0–139.2 nm. Binning these 30 bins into two channels improves the SNR by a factor of about 4 from 0.35 to 1.4. While this SNR is still low, the temperature signal in the LBH (2,0) band is now above the shot noise level. The results from PCA of simulated data of LBH disk emissions suggest that the ratio of the two spectral channels A and B that span a single LBH band (2,0) as defined above is sufficient to determine the change in T_{ci} .

Deleted: presents the procedure

Deleted: to determine

Deleted: procedure

Deleted: which is

Deleted: some

270 2. Apply an instrument model on the band model spectra data to calibrate for the instrument's wavelength resolution and wavelength registration.

3. Bin the band model data into channels A and B. Tabulate the relationship of the ratio, B/A, to temperature.

4. Compute ratio in observations from the LBH (2,0) band and determine T_{ci} by regressing observed ratio on the predetermined relationship between ratio and temperature.

275 The two-channel ratio has a number of benefits, most importantly, it can limit the impact of the following uncertainties: (1) uncertainty associated with LBH excitation and extinction processes that affect the absolute intensity of each band, and (2) uncertainty associated with instrument performance variations across the LBH band system. This technique to derive T_{ci} only requires measurement of the relative magnitudes between two spectral channels of ~0.5 nm resolution and a vibrational-rotational band model to map temperature to measurements. Measurement of a fully resolved, radiometrically calibrated LBH band system is not required nor is a forward model to produce absolute LBH intensity.

3.2 Sources of Error

285 There are two categories of error associated with determining physical parameters from observations: measurement error and representativeness error. Measurement error is the error associated with the measuring device while representativeness error is the difference between the observation and the physical model's representation of the observation (Rodgers, 2000). There are two dominant sources of systematic measurement error in T_{ci} stemming from variations in the instrument's wavelength registration and resolution. Figure 3 shows the error in T_{ci} as a function of the error in the modeled wavelength registration and the error in the wavelength resolution. It is apparent in Fig. 3 that a significant temperature error of about 50 K (5–10%) can occur if the errors exceed a hundredth of a nanometer level for the wavelength registration and a tenth of a nanometer level for wavelength resolution. A discussion on mitigating these two sources of systematic measurement error when deriving T_{ci} from GOLD data is provided in Section 4.1.

290 The predominant source of random measurement error that determines the precision in T_{ci} is shot noise. The T_{ci} random measurement error given the random error in photon counts provided in the GOLD LIC data is quantified using Monte Carlo (MC) samples of simulated T_{ci} derivations considering the viewing conditions and instrument performance (McClintock et al., 2020a,b). Particle background counts is at times an additional random noise source. For the case study with GOLD data, the particle backgrounds were low as indicated by the "High Background" flag in the Level 1C data and therefore this error source is not considered. The statistics of background counts and the associated temperature errors should be quantified for the general application of this technique to any period.

300 Sources of representativeness error in deriving T_{ci} are those that cause relative differences in the channel intensity other than temperature that are not captured in the vibrational-rotational band model. Photoabsorption by O_2 is one source to consider. There is only a 1.5% difference in the mean absorption cross section between the two channels that corresponds to a negligible difference in transmittance due to O_2 along the line-of-sight considering

Deleted: spectra

Deleted: ratio to

Deleted: as a look-up table

Deleted: <#>Compute B/A ratio on observations of the LBH (2,0) band and determine T_{ci} by linearly regressing observed B/A ratio on the predetermined relationship between B/A ratio and temperature. ¶

Deleted: <#> approach

Deleted: <#>both the low SNR of the temperature signal and

Deleted: In general,

Moved (insertion) [2]

Deleted: bias

Deleted: bias

Deleted: how these two sources of biases can be

Deleted: ed

Deleted: in deriving T_{ci}

Deleted: actual

Deleted: For the case study with GOLD data, the T_{ci} random measurement error associated with GOLD observations is quantified using Monte Carlo (MC) samples of simulated T_{ci} derivations considering the viewing conditions and instrument performance (McClintock et al., 2020a,b). An estimate of the errors using MC samples is provided along with case study results in Section 4.1.

the O₂ absorption cross section variation with temperature. Another source of representativeness error associated with the (2,0) band is due to the overlap of the bright (2,0) transition and the weak (5,2) transition. Inaccurate specification of the v'=2 and v'=5 vibrational population rates cause a slight change in shape of the band with respect to the observations that could be interpreted as a change in the rotational temperature. Figure 8 in Ajello et al. (2020) provides the v'=0–6 population rates and their uncertainties. These uncertainties are used to determine the associated error in the derived temperatures using the (2,0) band due to inaccurate specification of the v'=2 and v'=5 population rates. It is important to note that this representativeness error does not exist if the (1,1) or (2,3) bands are used in the derivation instead of the (2,0) band because the (1,1) and (2,3) bands are isolated from other LBH bands. However, these bands are also much weaker and suffer from significantly larger random error due to shot noise. Figure 4 shows the total random measurement error and representativeness error in T_{ci} using the (2,0) band. The representativeness error is a function of temperature and can range from 15 K at $T_{ci} = 400$ K to 48 K at $T_{ci} = 1200$ K. Random measurement error from shot noise is a function of the (2,0) band intensity with values of 20 and 50 K for a photon counts of 2500 and 500, respectively.

3.3 Interpretation of Column-integrated Temperature

Interpretation of column-integrated temperature, T_{ci} , is addressed using synthetic LBH disk emission observations generated by forward modeling WAM simulation results. The column-integrated temperature computed from synthetic observations is hereafter denoted as T_{ci}^S to contrast to T_{ci}^G computed from GOLD LBH disk emission data that is introduced later. To examine if T_{ci}^S can be attributed to a certain altitude we compare the WAM altitude with a temperature that most closely matches T_{ci}^S , denoted as $p_{\tau=1}^S$, to the pressure level at the peak of the LBH contribution function, $p_{\tau=1}$, where the LBH optical depth, τ , is unity. $p_{\tau=1}^S$ and $p_{\tau=1}$ are computed over the entire simulation period of 2–8 November 2018.

The LBH contribution function peak, $p_{\tau=1}$, changes with solar zenith angle (SZA) and observing zenith angle (OZA) as shown in Fig. 5. $p_{\tau=1}$ decreases in pressure (increases in altitude) for increases in SZA and OZA with a stronger dependence on SZA. Removing the OZA dependence, Fig. 6 shows there is a clear difference in $p_{\tau=1}^S$ and $p_{\tau=1}$ in their respective dependences on SZA ($p_{\tau=1}^S$ ranges $3 \times 10^{-5} - 5 \times 10^{-5}$ hPa and $p_{\tau=1}$ ranges $2 \times 10^{-5} - 5.5 \times 10^{-5}$ when SZA ranges $5^\circ - 70^\circ$). The weaker SZA dependence of $p_{\tau=1}^S$ can be explained by the FWHM of the contribution function that spans ~60 km at low SZA and ~90 km for high SZA (Laskar et al., 2020). The contribution function acts as an averaging kernel for temperature over these large vertical widths that tends to reduce the SZA effect. The net result is derived temperatures that are generally hotter than temperatures at $p_{\tau=1}$ ($p_{\tau=1}^S \leq p_{\tau=1}$) for low SZA and temperatures that are generally cooler than temperatures at $p_{\tau=1}$ ($p_{\tau=1}^S \geq p_{\tau=1}$) for high SZA. Figure 6 also shows variability in $p_{\tau=1}^S$ (up to 1.5×10^{-5} hPa or ~10 km for the simulation conditions) at a given SZA that reflects considerable variability in the vertical temperature structure within the width of the contribution function given varying forcing conditions.

Figure 6 reinforces that T_{ci} derived from the procedural steps specified in Section 3.1 is a column-integrated quantity, containing information from a larger altitude range of the lower-middle thermosphere than just

Moved up [2]: Figure 3 shows the bias in T_{ci} as a function of the error in the modeled wavelength registration and the error in the wavelength resolution. It is apparent in Fig. 3 that a significant bias of about 50 K (5–10%) can occur if the errors exceed a hundredth of a nanometer level for the wavelength registration and a tenth of a nanometer level for wavelength resolution. A discussion on how these two sources of biases can be mitigated in deriving T_{ci} from actual GOLD data is provided in Section 4.1.

Deleted: Reliance on only a small bandwidth of LBH emissions simplifies uncertainty quantification of T_{ci} derivations due to changes in instrument performance across the entire band system. There are still two dominant sources of systematic bias in T_{ci} stemming from variations in the instrument's wavelength registration and resolution. Figure 3 shows the bias in T_{ci} as a function of the error in the modeled wavelength registration and the error in the wavelength resolution. It is apparent in Fig. 3 that a significant bias of about 50 K (5–10%) can occur if the errors exceed a hundredth of a nanometer level for the wavelength registration and a tenth of a nanometer level for wavelength resolution. A discussion on how these two sources of biases can be mitigated in deriving T_{ci} from actual GOLD data is provided in Section 4.1.

Deleted: $z_{\tau=1}^S$

Deleted: altitude

Deleted: $z_{\tau=1}$, w

Deleted: altitude where

Deleted: $z_{\tau=1}^S$ and $z_{\tau=1}$

Deleted: 8

Deleted: 13

Deleted: and are shown in Fig. 4 with respect to solar SZA (black). For low SZA, T_{ci}^S is shown to match most to WAM temperatures at altitudes, $z_{\tau=1}^S$, that are 5–10 km higher (about 30–90 K hotter) than suggested by $z_{\tau=1}$. The gap between T_{ci}^S and temperature at $z_{\tau=1}$ becomes smaller as SZA increases. This dependence of the difference between $z_{\tau=1}^S$ and $z_{\tau=1}$ on SZA is explained by also considering the full-width-half-max (FWHM) of the contribution function. Figure 4 shows that the contribution function peaks at about 153 ± 2.5 km for SZA = 0° and about 185 ± 10 km for SZA = 75° . The FWHM associated with these contribution functions span about 120–180 km and about 160–250 km for the SZA = 0° and SZA = 75° cases, respectively (Laskar et al., 2020). In the case of SZA = 0° the FWHM spans an altitude range in the lower thermosphere with the steepest thermospheric temperature gradients resulting in a wide range of temperatures contributing to T_{ci}^S with a net effect of a higher apparent temperature than that at $z_{\tau=1}$. As SZA increases the FWHM spans an altitude range where the thermosphere becomes isothermal in the middle thermosphere result[... [2]

Deleted: 4

Deleted: furthermore

Deleted: indeed

440 at $p_{\tau=1}$. Perhaps, T_{ci} can be justified to be attributed to $p_{\tau=1}$ when measurement and representativeness errors exceed the gap between T_{ci} and the temperatures at $p_{\tau=1}$ at a given SZA and OZA. In general, specific pressure or altitude attribution of T_{ci} requires additional a priori knowledge of the thermospheric temperature profile.

Deleted: $z_{\tau=1}$

Deleted: altitude

Deleted: as demonstrated with T_{ci}^s derived from synthetic LBH disk emission observations wherein the a priori information is given by WAM simulations.

4 Case Study

445 The two-channel ratio approach to derive the column-integrated temperature is demonstrated using NASA GOLD Level 1C disk FUV emission data, T_{ci}^G , for the period of 2–8 November 2018 during which a small geomagnetic storm has occurred. Due to the lack of independent thermospheric temperature observations, the efficacy of this approach is validated through comparisons with GOLD Level 2 version 3 temperature product (T_{DISK}) and two-channel column-integrated temperatures computed from the synthetic observations using the WAM simulations (T_{ci}^s) as described in Section 2. T_{ci}^G and T_{DISK} are equivalent variables only differing in the approach. T_{ci}^G is also compared to NRLMSISE-00 temperatures sampled at the altitude at $p_{\tau=1}$ based on the SZA and OZA. This sampled MSIS temperature is denoted as T_{MSIS} . The approach is further corroborated through comparisons of the storm-time changes of T_{ci}^G to hemispherically integrated Joule heating rates (Q_{JH}) estimated from SuperDARN and ground-based magnetometer data using AMGeo, ESA SWARM mass density measurements at 460 km ($\rho_{SWARM}^{460 km}$) based on calculation from precise orbit determinations using the Global Positioning System receivers on the spacecraft, and GOLD Level 2 version 3 $\Sigma O/N_2$ product ($\Sigma O/N_2^G$). Section 4.1 provides a description of the GOLD LBH Level 1C disk emission data used in the T_{ci}^G derivation, Section 4.2 presents results comparing T_{ci}^G with T_{DISK} , T_{MSIS} , and T_{ci}^s , and Section 4.3 presents results comparing the storm time response of T_{ci}^G with Q_{JH} , $\rho_{SWARM}^{460 km}$, and $\Sigma O/N_2^G$. Table 1 defines each of the variable symbols introduced above.

Deleted: T_{ci}^G and T_{DISK} are equivalent variables only differing in the approach to integrated thermospheric temperature

Deleted: Note that version 2 of T_{DISK} is used in these comparisons presented in the paper.

460

4.1 GOLD LBH Disk Emission Data

GOLD observes the daytime FUV airglow from ~134–162 nm on Earth's disk between 6 and 23 UT from geostationary orbit at 47.5°W longitude (Eastes, 2020). GOLD produces a full disk image every ~30 minutes at a spatial resolution of 125×125 km by alternating between scans of the Northern and Southern hemisphere. The GOLD Level 1C radiance data with a spectral sampling of 0.04 nm are used to derive T_{ci}^G in this study. The GOLD Level 1C data is spatially binned by 2×2 (250×250 km spatial resolution) to improve the SNR by a factor of 2. Prior to deriving T_{ci}^G , efforts were made to reduce the impact of systematic biases that are present in version 2 of the GOLD Level 1C data product. Variations in wavelength registration along the GOLD detector are identified with the location of the LBH (2,0) band peak through fitting a log-normal distribution. Variations in wavelength resolution along the GOLD detector are identified with the FWHM of the OI 135.6 doublet through fitting a 2-gaussian distribution. Variations in the wavelength registration are identified by differencing the modeled peak wavelength given the fitted OI 135.6 doublet FWHM by the peak wavelength determined by fitting a log-normal distribution to the (2,0) band. Note that the degradation of the detector due to the strength of the OI 135.6 doublet can cause errors in the spectral resolution estimate, but significant degradation had not occurred by 2–8 November 2018. Corrections for wavelength registration and resolution are incorporated into Step 2 of the T_{ci} algorithm (see Section 3).

Deleted: 6:10 and 20:10 UTC

4.2 Comparing T_{ci}^G to T_{DISK} , T_{MSIS} , and T_{ci}^S

Figure 7 displays T_{ci}^G along with T_{DISK} , T_{MSIS} , and T_{ci}^S over Earth's disk viewed by GOLD for a five day window from 3–7 November 2018 at 15 UT, noon LT at the center of the disk (47.5°W, 0°N). A small geomagnetic storm has commenced the evening of 4 November and lasted through 5 November (Gan et al., 2020). On first inspection, T_{ci}^G and T_{DISK} show general agreement in the temperature amplitudes and in the morphological temperature response to geomagnetic activity over the disk. Note that there is slight banding near the equator in T_{ci}^G and T_{DISK} where the southern and northern hemisphere scans meet that is likely due to systematic errors at the top and bottom edge of the detector that were not completely corrected. T_{ci}^G and T_{MSIS} show some agreement in the temperature morphology over the disk but T_{MSIS} displays cooler temperatures particularly at low SZA and OZA where the emissions originate deeper in the thermosphere. There is agreement in the temperature morphology over the disk between T_{ci}^G and T_{ci}^S prior to the storm, but the storm-time response simulated by WAM, as manifest in T_{ci}^S , shows considerably higher temperatures in the mid- and high- latitudes and a longer post-storm recovery time in comparison to T_{ci}^G and T_{DISK} .

Figure 8 shows the mean bias difference (MBD) of T_{ci}^G from T_{DISK} , T_{MSIS} , and T_{ci}^S as a function of longitude (considering latitudes between $\pm 10^\circ$) and latitude (considering all longitudes viewed by GOLD) for 2–8 November 2018 at 15 UT. During this period the temperatures derived from observations (i.e., T_{ci}^G and T_{DISK}) exhibit globally similar temperatures while T_{MSIS} and T_{ci}^S exhibit globally cooler and warmer temperatures to these observations, respectively. The overall good agreement between T_{ci}^G and T_{DISK} relative to T_{MSIS} and T_{ci}^S is again apparent. T_{ci}^G and T_{DISK} show strong agreement near the center of the disk with an MBD less than 15 K (1-3%) increasing to a maximum of ~ 40 K (4-8%) near the disk edge. The slope of $T_{ci}^G - T_{DISK}$ with respect to latitude and longitude indicates T_{ci}^G has a stronger south-north and west-east temperature gradient than T_{DISK} . $T_{ci}^G - T_{ci}^S$ displays a similar west-east slope to $T_{ci}^G - T_{DISK}$ except for the region just west of the sub-solar point (-80° – -50° longitude) where T_{ci}^S is ~ 25 K cooler than T_{ci}^G .

The T_{ci}^G and T_{DISK} comparison is expanded in Fig. 9 to include all times in the range 7–22 UT for the period of 2–8 November 2018. It is clear in Fig. 9 that T_{ci}^G and T_{DISK} have very different dependencies on the viewing conditions determined by SZA and OZA. T_{ci}^G increases with both SZA and OZA with a stronger dependence on SZA. T_{DISK} increases with OZA but remains relatively uniform with SZA even decreasing slightly for $SZA > 25^\circ$. There are two likely explanations for the dependence of the derived temperature on viewing conditions: (1) The derived temperatures reflect real temperature changes with viewing conditions because of the contribution function peaking at different pressures (Fig. 5). (2) The derived temperatures reflect temperature biases with viewing conditions because of changes in the LBH emission intensity. Intensity decreases with increasing SZA due to reduced LBH excitation but increases with increasing OZA due to a larger airmass along the line-of-sight. To test which explanation best describes the dependence of T_{ci}^G and T_{DISK} on viewing conditions, Fig. 9 is correlated to the pressure at the peak of the LBH contribution function, $p_{\tau=1}$, (Fig. 5) and to the mean LBH intensity measured by GOLD over the same period as a function of SZA and OZA. T_{DISK} is weakly correlated ($R=-0.15$) with $p_{\tau=1}$ and

Deleted: 5

Deleted: about

Deleted: C

Deleted: November

Deleted: th

Deleted: 5th

Deleted: T_{ci}^G agrees most with T_{MSIS} in the morphological temperature response to geomagnetic activity over the disk. There is also good agreement in the temperature morphology over the disk between T_{ci}^G and T_{ci}^S prior to the storm, but the storm-time response simulated by WAM, as manifest in T_{ci}^S , shows considerably higher temperatures in the mid- and high- latitudes and a longer post-storm recovery time in comparison to T_{ci}^G as well as T_{MSIS} . T_{ci}^G and T_{DISK} show general agreement, particularly at low latitudes, but T_{DISK} exhibits a significant north-south temperature gradient and a relatively constant east-west gradient both of which are absent in T_{ci}^G as well as T_{MSIS} . Note that there is slight banding near the equator in T_{ci}^G where the southern and northern hemisphere scans meet that is likely due to systematic errors (see Section 3.2) at the top and bottom edge of the detector that were not completely corrected.

545 strongly correlated (R=0.72) with LBH intensity. In contrast, T_{ci}^G is strongly correlated (R=-0.86) with $p_{\tau=1}$ and
 weak-moderately correlated (R=-0.32) with LBH intensity. The stronger correlation between T_{ci}^G and $p_{\tau=1}$ compared
 to T_{DISK} and $p_{\tau=1}$ and weaker correlation between T_{ci}^G and LBH intensity compared to T_{DISK} and LBH intensity over
 this analysis period is suggestive that T_{ci}^G is more sensitive to real temperature changes as the probed pressures
 change with viewing conditions and less susceptible to biases due to a change in LBH intensity with viewing
 550 conditions. This is attributed to the fact that T_{ci}^G derivation does not require measurement of a fully resolved,
 radiometrically calibrated LBH band system nor a forward model to produce absolute LBH intensity. There is likely
 still biases in T_{ci}^G with LBH intensity as indicated by the weak-moderate correlation (R=-0.32), particularly at low
 intensities (high SZA) where shot noise can lead to positive biases up to 15 K in the two-channel ratio approach.

4.3 Storm Time Response

555 Figure 10 displays the response to a small geomagnetic storm in T_{ci}^G , Q_{JH} , $\rho_{SWARM}^{460 km}$, and $\Sigma O/N_2^G$, T_{ci}^G ,
 $\rho_{SWARM}^{460 km}$, and $\Sigma O/N_2^G$ are shown as percent differences from the quiet-time conditions on 2 November 2018. The
 global temporal evolution of these variables is in good agreement with each other and consistent with known storm
 time responses of thermospheric variables (e.g., Fuller-Rowell et al., 1994). A rise of magnetospheric energy influx
 as suggested by Q_{JH} leads to increased temperatures and upwelling of heavy molecular rich air in the high- and mid-
 560 latitudes as indicated by depletions of $\Sigma O/N_2^G$ (-40% near 50° latitude and -20% near -50° latitude) and
 enhancements of T_{ci}^G (-20% near ±50° latitude) and $\rho_{SWARM}^{460 km}$ (-250% near ±50° latitude). Enhancements of $\Sigma O/N_2^G$
 (20-30% near 30° latitude) in the low-latitudes suggests a subsequent development of downwelling following the
 pole to equator global circulation in response to the storm-time Joule heating rise. Global thermospheric expansion
 is also apparent on 5 November as suggested by an increase of T_{ci}^G and $\rho_{SWARM}^{460 km}$ over all latitudes. Note that the first
 565 detection of the temperature change was on the evening of 4 November when Joule heating rates have started to
 increase but are still relatively low (< 50 GW). The post-storm recovery times are also in good agreement and appear
 to be on the order of 2-3 days.

5 Conclusions

570 A new technique to derive thermospheric temperature from space-based disk observations of FUV airglow
 is presented. The technique uses a ratio of the emissions in two spectral channels that together span the Lyman-
 Birge-Hopfield (LBH) (2,0) band to determine the change in band shape with respect to a change in the rotational
 temperature of N₂. While this study focused on the LBH (2,0) band to derive thermospheric temperature, the
described technique can be applied to any LBH band or combination of bands. The derived temperature from this
 575 technique is shown to be a column-integrated property referred to as column-integrated thermospheric temperature.
 T_{ci} - T_{ci} should not be attributed to the peak of the LBH contribution function without consideration of the viewing
 conditions and T_{ci} derivation uncertainty. The definition of column-integrated thermospheric temperatures and other
 parameters used for comparison in the paper is given in Table 1. Specific findings of this work are as follows.

Deleted: Figure 6 shows the root mean squared difference (RMSD) and mean bias difference (MBD) of T_{ci}^G from T_{DISK} , T_{MSIS} , and T_{ci}^S that is computed for a 5° latitudinal bin. In general, there is agreement of T_{ci}^G with T_{DISK} , T_{MSIS} , and T_{ci}^S at low latitudes as suggested by the RMSD and MBD. The consistent -25 K MBD at low latitudes for each paired difference, $T_{ci}^G - T_{DISK}$, $T_{ci}^G - T_{MSIS}$, and $T_{ci}^G - T_{ci}^S$, suggests that there is an overall bias in T_{ci}^G likely due to wavelength registration and/or resolution errors. There are also small-scale fluctuations in MBD observed in each pair that suggests small systematic errors in T_{ci}^G .
 As expected from the results shown Fig. 5, there are significant changes in bias as a function of latitude for $T_{ci}^G - T_{DISK}$ (ranging from -50 K to 40 K) and $T_{ci}^G - T_{ci}^S$ (ranging from -145 K to -10 K). The good agreement with T_{MSIS} compared to the other variables is again apparent in Fig. 6 with an RMSD ranging from 60 K to 100 K (6-18%) that is near the level of the random measurement uncertainty for a certain latitude and a negative temperature bias that gradually increases from 0 K in the southern high latitudes to -45 K (4-8%) in the northern high latitudes. It is not known at this time if this latitudinal trend in bias can be attributed to systematic measurement errors that change along the detector, biased altitude sampling of NRLMSISE-00 temperatures, and/or if NRLMSISE-00 is not completely capturing the latitudinal temperature gradient during this period. Further investigation is required to reconcile such systematic biases between observations and models. For example, climatological comparisons of T_{ci}^G , T_{DISK} , T_{MSIS} , and T_{ci}^S along with TIMED GUVI derived temperatures over the full GOLD mission lifetime may likely shed light on this issue. This should be performed once version 3 of T_{DISK} is released which is expected to have significant improvements to version 2 used in this paper. Overall, the good agreement with T_{MSIS} over this time period demonstrates the validity in this two-channel ratio approach in probing thermospheric temperature using LBH disk emissions.

Deleted: 7

Deleted: The storm has started on 4 November 2018 and lasted to 5 November 2018 (Gan et al., 2020). T_{ci}^G , $\rho_{SWARM}^{460 km}$, and $\Sigma O/N_2^G$ are shown as percent differences from the quiet-time conditions on 2 November 2018.

Deleted: 5th

The LBH spectrum quantified with PCA of synthetic daytime LBH disk emission data is found to highly compressible (two principal components explain 99.9% of the variability). Analysis of the secondary principal component mode, that characterizes how the LBH temperature signal manifests as the change in band shape, substantiates the approach to bin a LBH spectral band into two channels such that the temperature-induced band shape change is best preserved. The study has shown that thermospheric temperatures can be derived from an observed two-channel ratio by using a precomputed relationship of the ratio to temperature from an LBH vibrational-rotational band model. In this two-channel ratio approach, representativeness errors originating from forward modeling are reduced because radiometrically calibrated LBH band intensities are not required in the derivation procedure, and negative impact of systematic measurement errors, stemming from variations across the band system in the instrument's wavelength registration and resolution, is reduced because a fully resolved LBH band system is not required.

The derived temperature from the two-channel approach can have significant systematic biases of about 50 K (5–10%) if the wavelength registration and resolution are not known to the hundredth of a nanometer level and tenth of a nanometer level, respectively, as shown in Fig. 3. In addition to these known sources of systematic biases, there is intrinsic random error in T_{ci} due primarily to shot noise and representativeness error due to misspecification of the $v'=2$ and $v'=5$ population rates in the vibrational-rotational band model. Random measurement error is estimated to be 20–50 K (3–8%) and representativeness error is estimated to be 15–30 K (2–5%) for the case study with GOLD L1C data.

In a case study for the period of 2–8 November 2018 during which a small geomagnetic storm has occurred, the temperatures derived from observations (i.e., T_{ci}^G and T_{DISK}) exhibit globally similar temperatures. T_{ci}^S is in good agreement with T_{ci}^G and T_{DISK} at low latitudes but exhibits considerably higher temperatures at mid- and high-latitudes during the storm response and T_{MSIS} exhibits globally cooler temperatures to the observations. However, there are clear differences between T_{ci}^G and T_{DISK} with respect to viewing conditions. There is stronger correlation between T_{ci}^G and $p_{\tau=1}$ ($R=-0.86$) compared to T_{DISK} and $p_{\tau=1}$ ($R=-0.14$) and weaker correlation between T_{ci}^G and LBH intensity ($R=-0.32$) compared to T_{DISK} and LBH intensity ($R=0.72$) over the analysis period. These differences highlight a potential benefit of the two-channel ratio approach to reduce representativeness error by measurement of the relative intensities between two channels that only requires a vibrational-rotational band model for the forward model instead of a full radiative transfer model. The temporal evolution of global T_{ci} corroborates well with temporal changes of hemispherically integrated Joule heating rates Q_{JH} , SWARM mass density at 460 km $\rho_{SWARM}^{460 km}$, and GOLD $\Sigma O/N_2^G$, which is consistent with known storm time responses of thermospheric variables.

Data Availability

The lookup table for the two-channel ratio versus N_2 rotational temperature considering the GOLD wavelength registration and resolution variation along the detector used to derive column-integrated temperatures and the resulting column-integrated temperatures for the period of November 2–8 2018 presented in this paper are available at <https://doi.org/10.17605/OSF.IO/KHNQ7>. GOLD L1C and L2 data can be accessed at the GOLD Science Data Center (<http://gold.cs.ucf.edu/search/>) and at NASA's Space Physics Data Facility (<https://spdf.gsfc.nasa.gov>). The

Deleted: The LBH temperature signal is quantified with PCA of synthetic daytime LBH disk emission data to be just 3% of the intensity of an LBH band and accounts for just 1.6% of the total variability in the simulated LBH disk emissions. The PCA result underscores the difficulty in extracting the thermospheric temperature signal from LBH disk emissions and the necessity of denoising efforts to improve the SNR. Analysis of the secondary principal component mode, that characterizes how the LBH temperature signal manifests as the change in band shape, substantiates the approach to bin a LBH spectral band into two channels such that the temperature-induced band shape change is best preserved. The SNR of the temperature signal is improved with the two channels compared to a fully resolved band.

Deleted: effectively eliminated

Deleted: absolute

Deleted: from shot noise

Deleted: This shot noise is estimated to be 50–95 K (5–15%) for the case of GOLD L1C data using MC simulations considering the viewing conditions and instrument performance as shown as gray dash line in Fig. 6. The derived temperature is, in general, a column-integrated property referred to as column-integrated thermospheric temperature, T_{ci} . T_{ci} should not be attributed to the peak of the LBH contribution function without consideration of SZA and T_{ci} derivation uncertainty. This is particularly true for low SZA, where the observed LBH emissions emanate from a region of sharp temperature gradients. Using a priori knowledge of the thermospheric temperature profile from WAM simulations, as shown in Section 3.2, T_{ci}^S matches most to temperatures at altitudes 5–10 km higher (about 30–90 K hotter) than at $z_{\tau=1}$ for low SZA. As SZA increases, the gap between T_{ci}^S and temperature at $z_{\tau=1}$ becomes smaller.

Deleted: In a case study for the period of 2–8 November 2018 during which a small geomagnetic storm has occurred, T_{ci} agrees with T_{MSIS} across the disk with a bias that spans from 0 to -45 K with latitude and to a lesser degree with GOLD Level 2 temperature product. At low latitudes T_{ci}^G agrees well with T_{DISK} , T_{ci}^S , and T_{MSIS} with a consistent mean-bias-difference of about -25 K. Mean-bias and root-mean-squared differences between $T_{ci}^G - T_{DISK}$ and $T_{ci}^G - T_{ci}^S$ vary with latitudes as well as geomagnetic activity levels.

Deleted: The derived column-integrated temperatures for the period of November 2–8, 2018 using the procedure presented in this paper are available at <https://doi.org/10.17605/OSF.IO/KHNQ7>.

code for NOAA's WAM model is available at <https://github.com/NOAA-SWPC/WAM>. The code for the NRLMSISE-00 neutral atmosphere model is available from the NASA CCMC, at <ftp://hanna.ccmc.gsfc.nasa.gov/pub/modelweb/atmospheric/msis/nrlmsise00/>. The Python interface for the NRLMSISE-00 neutral atmosphere model is available at <https://github.com/st-bender/pynrlmsise00>. Near-Earth solar wind data is provided by the Goddard Space Flight Center Space Physics Data Facility and is available at <https://omniweb.gsfc.nasa.gov/>. The density measurements (L2 DNSxPOD data product) from Swarm can be obtained through the web site at <https://earth.esa.int/web/guest/swarm/data-access> upon registration. AMGeO is an open source software available from amgeo.colorado.edu upon registration. SuperMAG ground magnetometer data is available at <https://supermag.jhuapl.edu/>. SuperDarn radar data is available at <http://vt.superdarn.org>.

710

715

Author Contribution

CC developed the presented technique and performed the analyses. TM contributed AMGeO, determined the validation approach and provided interpretation of the analyses. CC and TM prepared the manuscript.

720

Competing Interests

The authors declare that they have no conflict of interest.

Acknowledgements

The authors acknowledge W.E. McClintock for his assistance with the GOLD data, S. Solomon for his assistance with the use of GLOW model, A. Kubaryk for his assistance with the use of WAM, and L. Kilcommons for his assistance with the use of AMGeO. This work is supported by the NASA Future Investigator in NASA Earth and Space Sciences (FINESST) award 80NSSC19K1432. TM is supported by the NSF CAREER award AGS-1848544. AMGeO is supported by the NSF EarthCube awards ICER 1928403, ICER 1928327, and ICER 1928358. The authors acknowledge the use of SuperDARN data. SuperDARN is a collection of radars funded by national scientific funding agencies of Australia, Canada, China, France, Italy, Japan, Norway, South Africa, United Kingdom and the United States of America. For SuperMAG data we are grateful for INTERMAGNET, Alan Thomson; CARISMA, PI Ian Mann; CANMOS, Geomagnetism Unit of the Geological Survey of Canada; The S-RAMP Database, PI K. Yumoto and Dr. K. Shiokawa; The SPIDR database; AARI, PI Oleg Troshichev; The MACCS program, PI M. Engebretson; GIMA; MEASURE, UCLA IGPP and Florida Institute of Technology; SAMBA, PI Eftyhia Zesta; 210 Chain, PI K. Yumoto; SAMNET, PI Farideh Honary; IMAGE, PI Liisa Juusola; Finnish Meteorological Institute, PI Liisa Juusola; Sodankylä Geophysical Observatory, PI Tero Raita; UiT the Arctic University of Norway, Tromsø Geophysical Observatory, PI Magnar G. Johnsen; GFZ German Research Centre For Geosciences, PI Jürgen Matzka; Institute of Geophysics, Polish Academy of Sciences, PI Anne Neska and Jan Reda; Polar Geophysical Institute, PI Alexander Yahnin and Yarolav Sakharov; Geological Survey of Sweden, PI Gerhard Schwarz; Swedish Institute of Space Physics, PI Masatoshi Yamauchi; AUTUMN, PI Martin Connors; DTU Space, Thom Edwards and PI Anna Willer; South Pole and McMurdo Magnetometer, PI's Louis J. Lanzarotti and Alan T. Weatherwax; ICESTAR;

730

735

740

RAPIDMAG; British Antarctic Survey; MacMac, PI Dr. Peter Chi; BGS, PI Dr. Susan Macmillan; Pushkov Institute of Terrestrial Magnetism, Ionosphere and Radio Wave Propagation (IZMIRAN); MFGI, PI B. Heilig; 745 Institute of Geophysics, Polish Academy of Sciences, PI Anne Neska and Jan Reda; University of L'Aquila, PI M. Vellante; BCMT, V. Lesur and A. Chambodut; Data obtained in cooperation with Geoscience Australia, PI Andrew Lewis; AALPIP, co-Pis Bob Clauer and Michael Hartinger; SuperMAG, PI Jesper W. Gjerloev; Data obtained in cooperation with the Australian Bureau of Meteorology, PI Richard Marshall.

750 **References**

- Ajello, J. & Shemansky, Donald. (1985). A reexamination of important N₂ cross sections by electron impact with application to the dayglow: The Lyman-Birge-Hopfield Band System and N I (119.99 nm). *Journal of Geophysical Research*. 90. 9845-9861. doi:[10.1029/JA090iA10p09845](https://doi.org/10.1029/JA090iA10p09845).
- 755 Ajello, J. M., Evans, J. S., Veibell, V., Malone, C. P., Holsclaw, G. M., Hoskins, A. C., et al. (2020). The UV spectrum of the Lyman-Birge-Hopfield band system of N₂ induced by cascading from electron impact. *Journal of Geophysical Research: Space Physics*, 125, e2019JA027546. <https://doi.org/10.1029/2019JA027546>
- Akmaev, R. A. (2011). Whole atmosphere modeling: Connecting terrestrial and space weather, *Reviews of Geophysics*, 49, RG4004. doi:[10.1029/2011RG000364](https://doi.org/10.1029/2011RG000364).
- Aksnes, A., Eastes, R., Budzien, S., and Dymond, K. (2006). Neutral temperatures in the lower thermosphere from N₂ Lyman-Birge-Hopfield (LBH) band profiles, *Geophysical Research Letters*, 33, L15103. doi:[10.1029/2006GL026255](https://doi.org/10.1029/2006GL026255).
- 765 AMGeO Collaboration (2019). A Collaborative Data Science Platform for the Geospace Community: Assimilative Mapping of Geospace Observations (AMGeO) v1.0.0. Zenodo. <http://doi.org/10.5281/zenodo.3564914>.
- 770 Astafyeva, E., Zakharenkova, I., Huba, J. D., Doornbos, E., & van den Ijssel, J. (2017). Global Ionospheric and thermospheric effects of the June 2015 geomagnetic disturbances: Multi-instrumental observations and modeling. *Journal of Geophysical Research: Space Physics*, 122, 11, 716-11,742. <https://doi.org/10.1002/2017JA024174>.
- 775 Budzien, S. A., Fortna, C. B., Dymond, K. F., Thonnard, S. E., Nicholas, A. C., McCoy, R. P., & Thomas, R. J. (2001). Thermospheric temperature derived from ARGOS observations of N₂ Lyman-Birge-Hopfield emission. 2001 AGUSM SA62A03B.

- 780 Cantrall, C. E., Matsuo, T., & Solomon, S. C. (2019). Upper atmosphere radiance data assimilation: A feasibility study for GOLD far ultraviolet observations. *Journal of Geophysical Research: Space Physics*, 124, 8154– 8164. <https://doi.org/10.1029/2019JA026910>.
- Christensen, A. B., et al. (2003). Initial observations with the Global Ultraviolet Imager (GUVI) in the NASA TIMED satellite mission, *Journal of Geophysical Research: Space Physics*, 108, 1451, doi:[10.1029/2003JA009918](https://doi.org/10.1029/2003JA009918), A12.
- 785 Correia, J, Evans, J. S., Krywonos, A., Lumpe, J. D., Codrescu, M., Veibell, V., McClintock, B. E., & Eastes, R. (2018). Global-scale Observations of Limb and Disk (GOLD): Overview of O/N₂ and QEV science data products. Abstract SA21A-3169 presented at 2018 AGU Fall Meeting, Washington, DC. 10–14 Dec.
- 790 Eastes, R. W. (2000a). Emissions from the N₂ Lyman-Birge-Hopfield bands in the Earth's atmosphere, *Physics and Chemistry of the Earth, Part C: Solar, Terrestrial & Planetary Science*, 25(5–6), 523– 527. [https://doi.org/10.1016/S1464-1917\(00\)00069-6](https://doi.org/10.1016/S1464-1917(00)00069-6).
- Eastes, R. W. (2000b). Modeling the N₂ Lyman-Birge-Hopfield bands in the dayglow: Including radiative and collisional cascading between the singlet states, *Journal of Geophysical Research: Space Physics*, 105(A8), 18557– 18573, doi:[10.1029/1999JA000378](https://doi.org/10.1029/1999JA000378).
- 795 Eastes, R.W., McClintock, W.E., Codrescu, M.V., Aksnes, A., Anderson, D.N., Andersson, L., et al. (2008). Global-Scale Observations of the Limb and Disk (GOLD): New Observing Capabilities for the Ionosphere-Thermosphere. In Midlatitude Ionospheric Dynamics and Disturbances (eds P.M. Kintner, A.J. Coster, T. Fuller-Rowell, A.J. Mannucci, M. Mendillo and R. Heelis). <https://doi.org/10.1029/181GM29>.
- 800 Eastes, R.W., McClintock, W.E., Burns, A.G. et al. (2017). The Global-Scale Observations of the Limb and Disk (GOLD) Mission. *Space Science Reviews* 212, 383–408. <https://doi.org/10.1007/s11214-017-0392-2>.
- 805 Fuller-Rowell, T. J., Codrescu, M. V., Moffett, R. J., and Quegan, S. (1994). Response of the thermosphere and ionosphere to geomagnetic storms, *Journal of Geophysical Research*, 99(A3), 3893–3914, doi:[10.1029/93JA02015](https://doi.org/10.1029/93JA02015).
- 810 Gan, Q., Eastes, R. W., Burns, A. G., Wang, W., Qian, L., Solomon, S. C., et al. (2020). First synoptic observations of geomagnetic storm effects on the global-scale OI 135.6-nm dayglow in the thermosphere by the GOLD mission. *Geophysical Research Letters*, 47, e2019GL085400. <https://doi.org/10.1029/2019GL085400>.

- Laskar, F. I., Pedatella, N. M., Codrescu, M. V., Eastes, R. W., Evans, J. S., Burns, A. G., & McClintock, W. (2021). Impact of GOLD retrieved thermospheric temperatures on a whole atmosphere data assimilation model. *Journal of Geophysical Research: Space Physics*, 126, e2020JA028646. <https://doi.org/10.1029/2020JA028646>.
- 815
- Matsuo T. (2020), Recent Progress on Inverse and Data Assimilation Procedure for High-Latitude Ionospheric Electrodynamic. In: Dunlop M., Lühr H. (eds) Ionospheric Multi-Spacecraft Analysis Tools. *ISSI Scientific Report Series*, vol 17. Springer, Cham. https://doi.org/10.1007/978-3-030-26732-2_10.
- 820
- McClintock, W. E., Eastes, R. W., Hoskins, A. C., Siegmund, O. H. W., McPhate, J. B., Krywonos, A., et al. (2020a). Global-scale observations of the limb and disk Mission implementation: 1. Instrument design and early flight performance. *Journal of Geophysical Research: Space Physics*, 125, e2020JA027797. <https://doi.org/10.1029/2020JA027797>.
- 825
- McClintock, W. E., Eastes, R. W., Beland, S., Bryant, K. B., Burns, A. G., Correia, J., et al. (2020b). Global-scale observations of the limb and disk mission implementation: 2. Observations, data pipeline, and level 1 data products. *Journal of Geophysical Research: Space Physics*, 125, e2020JA027809. <https://doi.org/10.1029/2020JA027809>.
- 830
- Mende, S.B., Frey, H.U., Rider, K. et al. (2017). The Far Ultra-Violet Imager on the Icon Mission. *Space Science Reviews* 212, 655–696. <https://doi.org/10.1007/s11214-017-0386-0>.
- Meier, R.R. (1991). Ultraviolet spectroscopy and remote sensing of the upper atmosphere. *Space Science Reviews* 58, 1–185. <https://doi.org/10.1007/BF01206000>.
- 835
- Paxton, L.J., Morrison, D., Zhang, Y., Kil, H., Wolven, B., Ogorzalek, B.S., et al. (2002). Validation of remote sensing products produced by the Special Sensor Ultraviolet Scanning Imager (SSUSI): a far UV-imaging spectrograph on DMSP F-16. *Proc. SPIE 4485, Optical Spectroscopic Techniques, Remote Sensing, and Instrumentation for Atmospheric and Space Research IV*. <https://doi.org/10.1117/12.454268>
- 840
- Paxton, L. J., Schaefer, R. K., Zhang, Y., and Kil, H. (2017). Far ultraviolet instrument technology, *Journal of Geophysical Research: Space Physics*, 122, 2706–2733, doi:[10.1002/2016JA023578](https://doi.org/10.1002/2016JA023578).
- Picone, J. M., Hedin, A. E., Drob, D. P., and Aikin, A. C. (2002). NRLMSISE-00 empirical model of the atmosphere: Statistical comparisons and scientific issues, *Journal of Geophysical Research: Space Physics*, 107(A12), 1468, doi:[10.1029/2002JA009430](https://doi.org/10.1029/2002JA009430).
- 845
- Rodgers, C. D. (2000). Inverse methods for atmospheric sounding: Theory and practice. Singapore: World Scientific.

850

Solomon, S. C. (2017). Global modeling of thermospheric airglow in the far ultraviolet, *Journal of Geophysical Research: Space Physics*, 122, 7834– 7848, doi:[10.1002/2017JA024314](https://doi.org/10.1002/2017JA024314).

855

Strickland, D. J., Evans, J. S., and Paxton, L. J. (1995). Satellite remote sensing of thermospheric O/N₂ and solar EUV: 1. Theory, *Journal of Geophysical Research: Space Physics*, 100(A7), 12217– 12226, doi:[10.1029/95JA00574](https://doi.org/10.1029/95JA00574).

860

Visser, P., Doornbos, E., van den IJssel, J. et al. (2013). Thermospheric density and wind retrieval from Swarm observations. *Earth, Planets and Space* 65, 12 <https://doi.org/10.5047/eps.2013.08.003>.

865

Zhang, Y., Paxton, L. J., & Schaefer, R. K. (2019). Deriving thermospheric temperature from observations by the global ultraviolet imager on the thermosphere ionosphere mesosphere energetics and dynamics satellite. *Journal of Geophysical Research: Space Physics*, 124, 5848– 5856. <https://doi.org/10.1029/2018JA026379>.

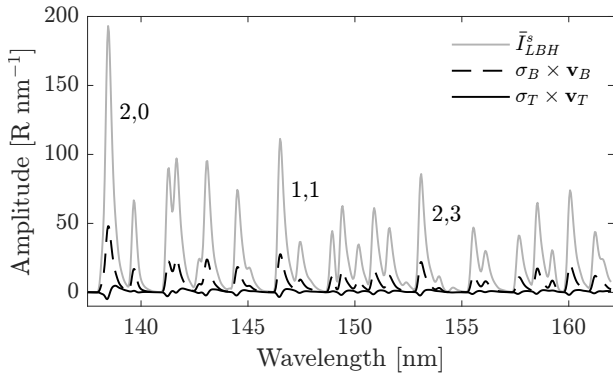
870

Tables and Figures

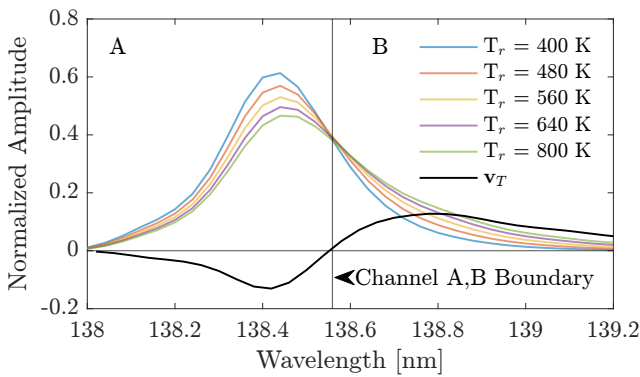
T_{ci}^G	Column-integrated thermospheric temperature derived from GOLD LIC disk data
T_{ci}^S	Column-integrated thermospheric temperature derived from simulated disk data
T_{DISK}	GOLD Level 2 version 2 thermosphere temperature product
T_{MSIS}	MSIS temperature at the altitude $z_{T_{ci}^S}$ (See Fig. 4)
Q_{IH}	AMGeO hemispherically integrated Joule heating rate
$\rho_{SWARM}^{460 km}$	SWARM A mass density at 460 km
$\Sigma O/N_2^G$	GOLD Level 2 version 2 column O/N ₂ ratio

Table 1: Definitions of symbols

875

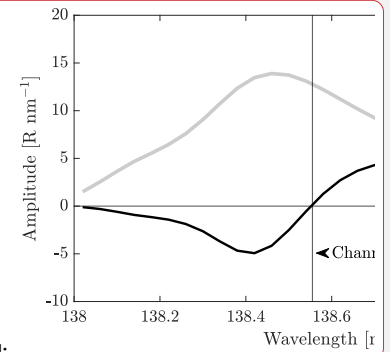


880 **Figure 1:** Simulated top-of-atmosphere mean LBH emissions (gray), T_{LBH}^s , and the principal components associated with overall brightening of emissions (dashed black), v_B , and the temperature signal (solid black), v_T , scaled by their respective eigenvalues, σ_B and σ_T . These two principal components account for 99.9% of the variability about the mean for the period of 2–8 November 2018.

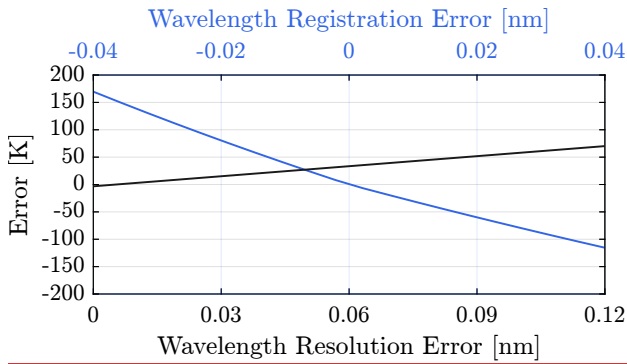


885 **Figure 2:** The second principal component (black line), v_T , over the LBH (2,0) band and the normalized amplitude of the LBH (2,0) band at five N_2 rotational temperatures, T_r . Emissions at 138.56 nm, where v_T changes the sign, are independent of temperature, and provide a boundary to split the (2,0) band into channels A and B.

Deleted: Simulated top-of-atmosphere mean LBH emissions (gray), T_{LBH}^s , and the principal components associated with overall brightening of emissions (dashed black), v_B , and the temperature signal (solid black), v_T , scaled by their respective eigenvalues, σ_B and σ_T . These two principal components account for 99.9% of the variability about the mean. σ_B^2 accounts 98.3% of the total variability in the LBH emissions and σ_T^2 accounts for 1.6% of the total variability in the simulated LBH emissions over the entire disk over the period of November 2–8, 2018.

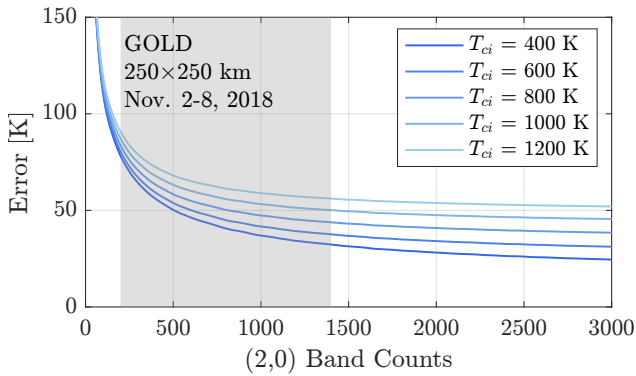


Deleted: Principal component associated with temperature (black line), v_T , over the LBH (2,0) band scaled by the eigenvalue, σ_T . v_T represents an effective skewing of the emission feature to longer wavelengths or shorter wavelengths. Emissions at 138.56 nm, where v_T changes the sign, are unaffected by v_T (i.e., independent of temperature), and provide a boundary location to divide the (2,0) band into channels A and B. The shot noise level (gray) that is the dominant random noise source is also shown.



915

Figure 3: Expected bias errors in T_{ci} as a function of the two dominant known sources systematic measurement errors: the instrument's wavelength registration (blue) and variations in the wavelength resolution (black).



920

Figure 4: Total T_{ci} random measurement error (not including particle noise) and representativeness error for the (2,0) band. The range of (2,0) band counts for GOLD data (250 × 250 km resolution at nadir) used in the case study in Section 4 is highlighted by the grey box.

925

Deleted: Expected bias errors in T_{ci} as a function of varying degrees of the two dominant known sources systematic measurement errors: the instrument's wavelength registration (red) and variations in the wavelength resolution (black).

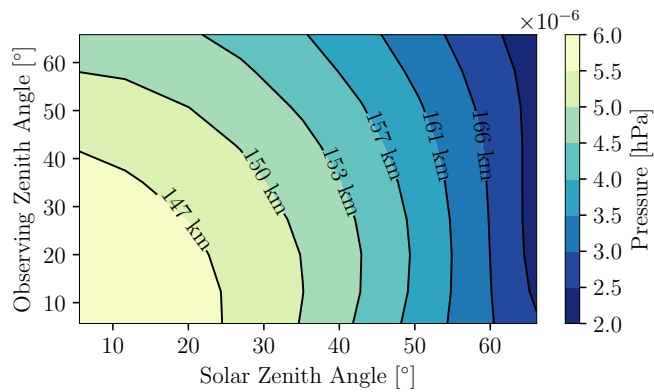
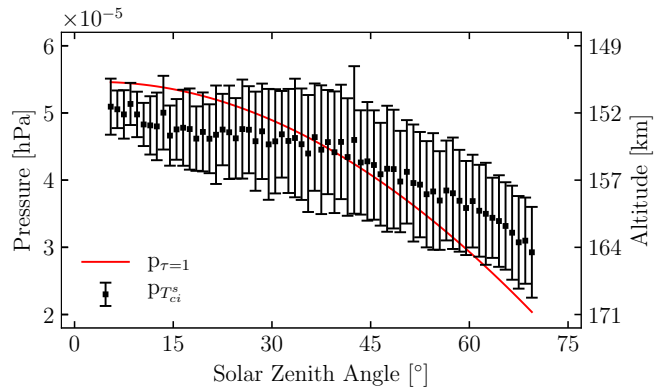
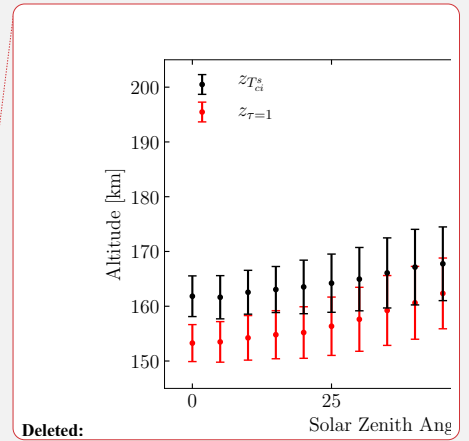


Figure 5: Pressure at the peak of the LBH contribution function, $p_{\tau=1}$, as a function of SZA and OZA determined from forward modeling WAM simulations for the period of 2-8 November 2018 considering realistic forcing conditions. LBH emissions are on constant pressure level surfaces given the solar and observing zenith angles. Approximate corresponding altitudes in the WAM simulations are also provided but note that these altitudes will vary depending on the forcing conditions.

935



940



Deleted:

Figure 6: The mean and standard deviation of the pressure for the simulated WAM temperature that is closest to T_{ci}^s , as a function of SZA averaged over all OZA for the simulation period of 2–8 November 2018 (black). The peak of the LBH contribution function, $p_{\tau=1}$, is shown as a function of SZA based on forward modeling of LBH disk emissions using the same WAM simulation (red). This peak is constant with respect to pressure level for a given SZA and OZA.

Deleted: 4

Deleted: The mean and standard deviation of the altitude of the simulated WAM temperature that is closest to T_{ci}^s , $z_{T_{ci}^s}$, as a function of SZA over the simulation period of November 2–8, 2018 (black). The mean and standard deviation of the peak of the LBH contribution function, $z_{\tau=1}$, is also shown as a function of SZA based on forward modeling of LBH disk emissions using the same WAM simulation (red).

Deleted: The mean and standard deviation of the altitude of the simulated WAM temperature that is closest to T_{ci}^s , $z_{T_{ci}^s}$, as a function of SZA over the simulation period of November 2–8, 2018 (black). The mean and standard deviation of the peak of the LBH contribution function, $z_{\tau=1}$, is also shown as a function of SZA based on forward modeling of LBH disk emissions using the same WAM simulation (red).

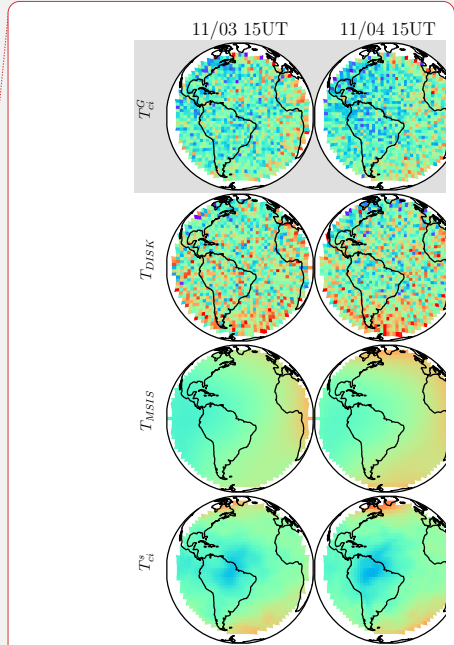
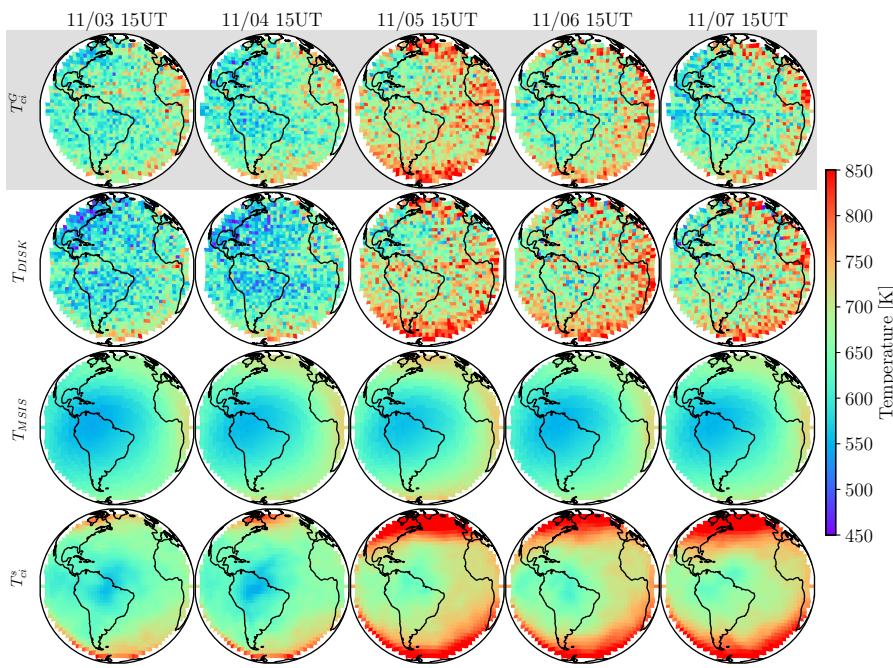


Figure 7: Comparison of T_{ci}^G with T_{DISK} , T_{MSI} , and T_0^s over Earth's disk viewed by GOLD for a five-day window from November 3–7, 2018 at about 15 UT, noon LT at the center of the disk (47.5°W, 0°N). A small geomagnetic storm has commenced the evening of 4 November, and lasted through 5 November.

Deleted:
 Deleted: 5
 Deleted: 4th
 Deleted: 5th

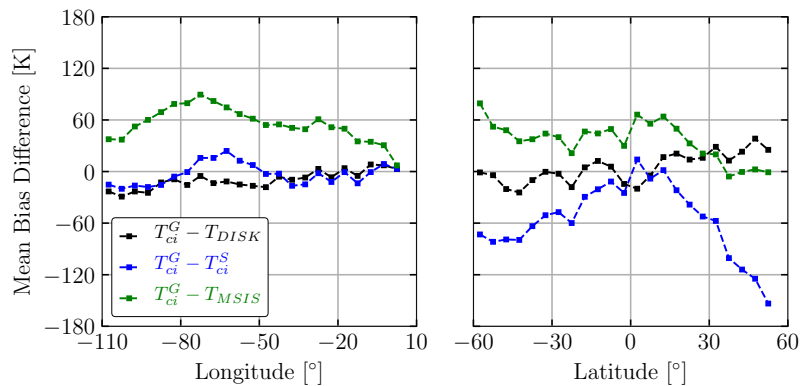
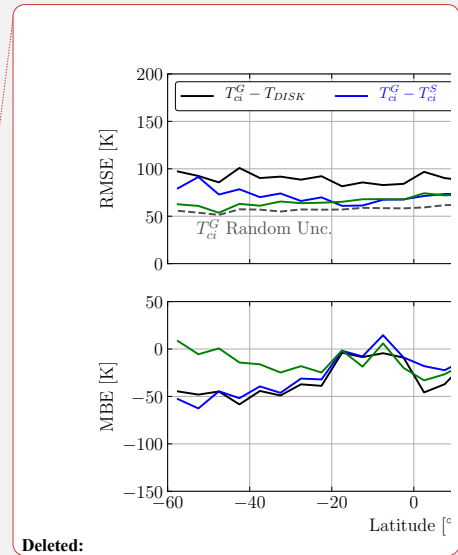


Figure 8: Mean bias difference (MBD) of T_{ci}^G from T_{DISK} , T_{MSIS} , and T_{ci}^S for 5° bins as a function of longitude (left) and latitude (right) during 2–8 November 2018 at 15 UT. All longitudes viewed by GOLD are considered when computing MBD as a function of latitude and only equatorial latitudes between $\pm 10^\circ$ are considered when computing MBD as a function of longitude.

970



Deleted:

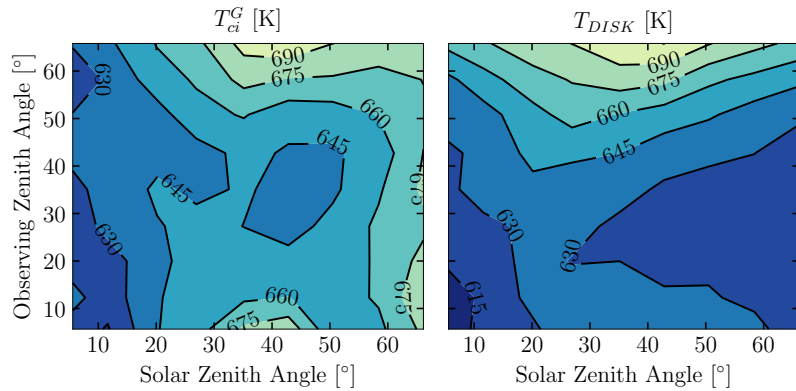
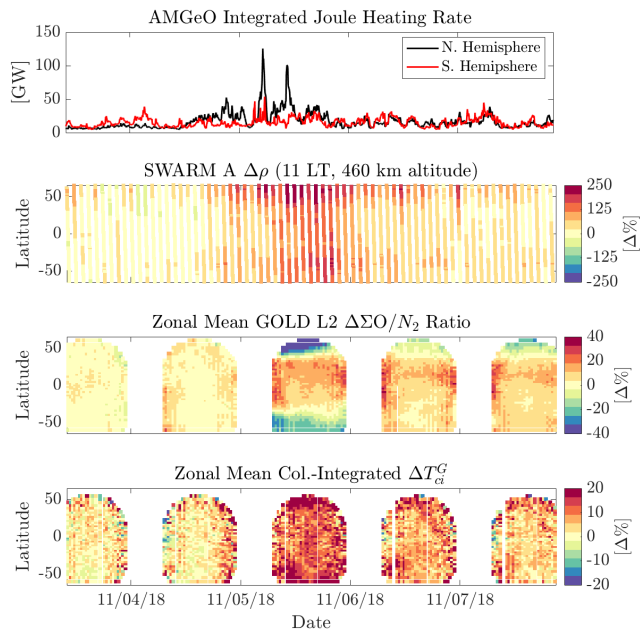


Figure 9: Mean T_{ci}^G and T_{DISK} temperatures as a function of SZA and OZA for the period of 2–8 November 2018 with 5° binning in SZA and OZA.

975



980 **Figure 7: Storm-time response of the thermosphere as observed in three thermospheric variables as well as the hemispherically integrated Joule heating estimated using AMGeO. The percent change in mass density, ($\Delta\rho_{SWARM}^{460 km}$), column O/N₂ ratio ($\Delta\Sigma O/N_2$), column-integrated temperature (ΔT_{ci}^G) are computed with quiet-time conditions on 2 November 2018.**

985

Deleted: Figure 6: Root mean squared difference (top) and mean bias difference (bottom) of T_{ci}^G from T_{DISK} , T_{MSIS} , and T_{ci}^s computed for a given latitude over the period of November 2–8, 2018. The random uncertainty in T_{ci}^G is also shown by the gray dashed line (top).

Deleted: 2nd,

| **Page 4: [1] Deleted** Clayton Cantrall 8/25/21 11:51:00 AM

| **Page 6: [2] Deleted** Clayton Cantrall 8/25/21 12:13:00 PM